

Overvoltage Calculation Method for Sending System Under DC Fault Disturbance Considering the Influence of Renewable Energy

Haoyue Gong, Jianbo Guo, *Senior Member, IEEE, Fellow, CSEE*, Qiang Guo, *Member, IEEE, Fellow, CSEE*, Jian Zhang, Qinyong Zhou, and Libo Zhang

Abstract—Bipolar blocking and commutation failure in the renewable energy transmission system through ultra-high voltage direct current will produce significant temporary overvoltage. This paper analyzes the physical process of sending end grid overvoltage caused by two types of DC faults and establishes a DC overvoltage model considering renewable energy sources. According to characteristics of the sending end grid, the influence of the system equivalent impedance, the proportion of renewable energy output, the active and reactive power coefficients of the renewable energy sources during the low voltage ride through process on the overvoltage is analyzed respectively, and the relationship between the proportion of renewable energy output and the short-circuit ratio under the overvoltage constraint is constructed. The validity and practicality of the model and analysis method proposed in this paper are verified by combining the typical transmission system at the sending end of the actual power grid and regional power grid systems.

Index Terms—Bipolar blocking, commutation failure, low voltage ride through, renewable energy, temporary overvoltage.

I. INTRODUCTION

IN recent years, large-scale development of renewable energy represented by wind power and photovoltaics in north-west China has effectively supported the goals of “carbon peak and carbon neutrality” [1]. Ultra-high voltage direct current (UHVDC) transmission technology plays an important role in the outbound transmission of renewable energy due to its ability to transmit electricity over long distances on a large scale [2]–[4].

A converter station at the sending end of the direct current (DC) system typically has weaker voltage support capability. After significant power disturbances occur, fluctuations in the converter bus voltage can be substantial [5], [6]. To ensure safe and stable operation of the system, equipping the sending end’s nearby area with a certain capacity of synchronous generating units [7] can effectively suppress the phenomenon of power frequency temporary overvoltage (TOV) caused by

the obstruction of active power transmission [8]. For DC systems integrating renewable energy sources (RESs) with synchronous generators for bundled transmission, existing studies have shown the ratio of the two types of power sources connected affects the TOV at the converter bus differently. Regarding the TOV phenomenon at the sending end, there are already some studies analyzing TOV caused by bipolar blocking (BB) and commutation failure (CF).

Regarding BB faults, [9] analyzed the TOV level at the DC sending end converter bus after power disturbances from the perspective of surplus reactive power at the converter bus and the short-circuit ratio (SCR). Reference [10] focused on the DC transmission systems that integrate wind and solar power for bundled transmission, analyzing the causes and mitigation measures for TOV at the converter bus triggered by BB fault. Reference [11] based on the post-disturbance system power flow, analyzed the TOV phenomenon in wind and thermal power bundled transmission, the mechanism of wind turbine units disconnecting due to high voltage, and the solutions. Reference [12] equivalently modeled the DC transmission system and used the SCR to characterize the system’s voltage support strength at the converter bus, quantitatively analyzing the range of the SCR of the sending end converter bus under TOV non-exceedance conditions. Reference [13], building on [9], further considered the effect of increased reactive power output from capacitors due to voltage rise in the calculation of TOV. Reference [14] quantitatively calculated the TOV conditions at converter bus under both unipolar and BB by using the SCR and power flow results.

For CF faults, reference [15] quantitatively calculated the TOV at the sending end converter bus following a CF. Reference [16] calculated the TOV level at the converter bus after CF by analyzing the longitudinal and transverse components in the power flow results. References [17] and [18] analyzed the TOV at the converter bus after CF, respectively, using a voltage index and the dynamic process of the DC system post-fault. Reference [19] innovatively quantified the TOV at the converter bus following disturbances such as BB and CF using a unified expression for quantitative calculation.

Although the aforementioned references have achieved quantitative calculation of TOV at the DC sending end from various aspects, it has not yet considered the impact of the proportion of RES integration or dynamic control parameters of RES on TOV.

Manuscript received January 17, 2023; revised March 22, 2023; accepted April 28, 2023. Date of online publication February 27, 2024; date of current version March 19, 2024. This work was supported by the National Key R&D Program of China (2022YFB2403100).

H. Y. Gong (corresponding author, email: yjs-ghy@epri.sgcc.com.cn), J. B. Guo, Q. Guo, J. Zhang, Q. Y. Zhou and L. B. Zhang are with China Electric Power Research Institute, Beijing 100192, China.

DOI: 10.17775/CSEEJPES.2023.00290

Reference [20] combined the dynamic characteristics of wind turbine units with the distribution of power flow before and after disturbances to analyze the TOV situation at the DC sending end bus under BB and CF. References [21] and [22], taking the key control parameters during the low voltage ride-through (LVRT) period of RES as the entry point, studied the impact of the dynamic characteristics of RES on the TOV at the DC's sending end, respectively, proposing analyses of the impact level of LVRT parameters and optimization strategies.

The aforementioned references have made commendable attempts in analyzing the mechanism of TOV at the converter bus in renewable energy export systems, but the majority have only engaged in qualitative analysis. In the context of grid planning and actual operation, there is a desire to obtain quantitative calculations of TOV at the converter bus, thereby supporting decision-making for the startup of synchronous power sources and rational analysis of RES integration. However, to date, there have been no reports on quantitative calculations of TOV at the DC's sending end that involve the integration ratio of RES or control parameters.

This article builds upon the quantitative calculation of TOV following BB and CF faults, integrating the proportion of RES integration and dynamic control parameters, to achieve calculation of TOV at the converter bus. Compared to existing research results, this approach is more in line with the actual conditions of the power grid. Based on quantitative calculations, by analyzing the main factors affecting TOV, the paper proposes optimized decision-making recommendations for suppressing the level of TOV.

This paper presents a method for calculating TOV at the sending-end converter bus under various DC fault disturbances. The method takes into account factors such as the proportion of RES integration, SCR, and dynamic control coefficients during the LVRT period of the RES, achieving analytical calculation of the sending-end TOV.

The rest of this article is divided into four sections. Section II describes the existing calculation methods, and derives the quantitative calculation of the TOV of the converter bus after BB and CF, respectively. Section III carries out the sensitivity analysis of various parameters affecting the TOV, and produces an evaluation method of the TOV by combining the SCR of the converter bus, and the proportion of RES access. Section IV verifies the accuracy and practicability of the proposed calculation and evaluation method in typical sending-end system examples and actual power grid examples. A summary of findings and conclusions of this work are presented in Section V.

II. ANALYSIS OF LARGE DISTURBANCE TOV AT DC'S SENDING END

A. Introduction of Existing Analysis Methods

TOV of the DC system's sending end bus is usually caused by BB and CF. Consequently, analyzing the TOV of the converter bus involves examining the system's power flow changes following a significant DC fault. Typical DC-sending systems can be represented by the structure depicted in Fig. 1.

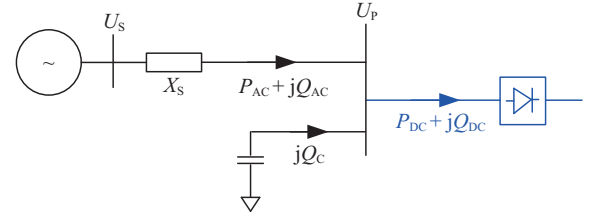


Fig. 1. Typical power flow of DC's sending end.

In Fig. 1, U_S and X_S are the voltage and the impedances of the equivalent power supply, and denoting U_P is the voltage of the converter bus. The apparent power supplied by the U_S to the converter bus is $P_{AC} + jQ_{AC}$, with $P_{DC} + jQ_{DC}$ denoting the apparent power flowing into the converter valve. The AC filter bank provides Q_C as capacitive reactive power at steady-state.

Reference [9] calculates TOV of BB fault by using the surplus reactive power ΔQ_C and the converter bus's short circuit capacity S_{SC} . The voltage rise of converter bus ΔU_P can be expressed as:

$$\Delta U_P = \frac{\Delta Q_C}{S_{SC}} \quad (1)$$

In [13], the relationship between the voltage rise after BB, and the reactive power output of the filter, as well as the reactive power exchange power Q_{ac} between AC and DC systems is proposed. Based on that, (1) is improved to obtain:

$$\Delta U_P = \frac{(1 + \Delta U_P)^2 \Delta Q_C + Q_{ac}}{S_{SC}} \quad (2)$$

The TOV of the DC system can be obtained by solving the quadratic equation of ΔU_P by (2).

In [16], employing converter's TOV transverse and longitudinal components and its reactive power demand Q_r during CF, the equation for post-fault converter bus voltage, U_F , is formulated as:

$$U_F \approx U_S + \frac{X_S}{U_S} \left[\left(\frac{U_F}{U_P} \right)^2 Q_C - Q_r \right] \quad (3)$$

Existing quantitative analysis methods for BB and CF in DC systems regard all kinds of power sources in the system as equivalent voltage sources with impedance, ignoring the characteristics of all kinds of RES as current sources. For all kinds of analysis of RES entering LVRT caused by CF of DC system, most are only analyzed from a qualitative perspective. Quantitative analysis of TOV based on various control parameters during LVRT of RES have not been reported in the literature. Therefore, we focus on the analysis of the TOV characteristics under BB and CF in the near field of DC transmission with RES.

B. Steady State Power Flows With RES

To further elaborate on the system depicted in Fig. 1, the equivalent power source can be decomposed into a RES and an equivalent power source for synchronous units, as shown in Fig. 2.

In steady state, the grid-connected bus voltage of the RES is U_W , injecting power $P_W + jQ_W$ into the converter bus. Bus

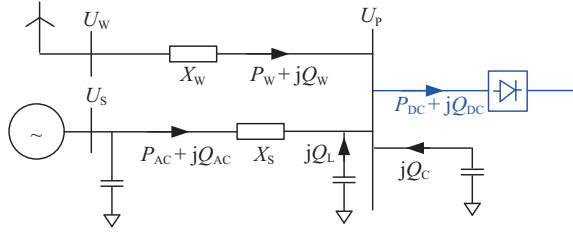


Fig. 2. Typical power flow with RES of DC's sending end.

voltage of the equivalent power source for synchronous units is U_S , providing the AC system with an apparent power of $P_{AC} + jQ_{AC}$. By defining the output ratio of the new energy source as the proportion of its active power output to the rated capacity of the DC system, represented by η_{RE} , the following can be obtained

$$P_W = \eta_{RE} P_{DC} \quad (4)$$

Transmission lines from the new energy sources and the equivalent synchronous generator are modeled using a Π -type equivalent, where Q_L represents the total equivalent AC system at the converter bus.

C. Sending-end Power Flow After Disturbance

For BB and CF, the TOV at the converter bus following both types of disturbances is attributed to the surplus reactive power from the filters. As analyzed in the relevant references, DC system sending end's converter valves require a substantial amount of reactive power during normal operation. The filters connected to the converter bus can essentially meet the reactive power demands of the converter valves, resulting in the AC system providing minimal reactive power to the converter bus. However, following BB and CF, there is a significant reduction in both the active power output of the DC transmission and the reactive power demand of the converter valves, leading to a considerable surplus of reactive power from the filters, which causes a sudden increase in voltage at the converter bus. Nevertheless, the dynamic characteristics of RES differ significantly during and after these two types of disturbances. In the case of CF, a certain amount of RES in the vicinity of the DC sending end will enter the LVRT, thereby limiting the export of active power and increasing reactive power to support the voltage. In contrast, during BB, there is no engagement in the LVRT, which is a primary factor contributing to the different levels of overvoltage following these disturbances.

To quantitatively represent active and reactive power output of the RES during the LVRT, the following can be derived:

$$P_{WF} = k_P P_W \quad (5)$$

$$Q_{WF} = k_Q P_W \quad (6)$$

where k_P and k_Q represent the coefficients for active and reactive power, respectively, of new energy sources during the LVRT.

Following the fault, the power flow in the vicinity of the DC system sending end is shown in Fig. 3. Q_{CF} denotes the reactive power injected by filters into the AC system after the disturbance, Q_{LF} represents the total equivalent reactive power

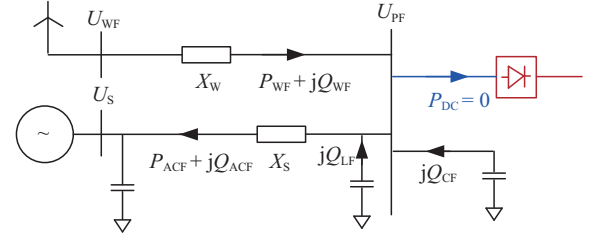


Fig. 3. Typical power flow after the disturbances of the DC system.

of the AC system after the disturbance, and $P_{ACF} + jQ_{ACF}$ indicates the power flowing into the equivalent synchronous generator. Considering capacitive reactive power is directly proportional to the square of the voltage, the relationship between the reactive power of the filters and the line before and after the fault can be described as follows:

$$Q_{CF} = Q_C \left(\frac{U_{PF}}{U_P} \right)^2 \quad (7)$$

$$Q_{LF} = Q_L \left(\frac{U_{PF}}{U_P} \right)^2 \quad (8)$$

As concluded in the references [15] and [16], let k_{DC} denote the reactive power calculation coefficient required for the operation of the converter bus after commutation failure. The reactive power injected into the equivalent synchronous generator can be derived through relevant power flow calculations as follows:

$$Q_{ACF} = (1 - k_{DC})Q_{CF} + Q_{LF} + Q_{WF} - \frac{P_{WF}^2 + [(1 - k_{DC})Q_{CF} + Q_{LF} + Q_{WF}]^2}{U_S^2} X_S \quad (9)$$

Furthermore, U_{PF} denotes as the bus voltage after fault, which can be calculated as follow:

$$U_{PF} = \sqrt{\left(U_S + \frac{Q_{ACF} X_S}{U_S} \right)^2 + \left(\frac{P_{ACF} X_S}{U_S} \right)^2} \quad (10)$$

Considering substituting (9) into (10) results in a quartic equation in terms of U_{PF} , the computational effort for solving it in engineering practice is considerable. When X_S is relatively small and the error is within an acceptable range, (11) can be used as an approximation to replace (9), as following:

$$Q_{ACF} \approx (1 - k_{DC})Q_{CF} + Q_{LF} + Q_{WF} - \frac{P_{WF}^2}{U_S^2} X_S \quad (11)$$

If the resistance in each transmission line is neglected and it is approximately assumed $P_{WF} = P_{ACF}$, by substituting (4) to (8) and (11) into (10), the following can be obtained:

$$U_{PF} = \left(\left(\frac{\eta_{RE}^2 P_{DC}^2 k_P^2 X_S}{U_S} \right)^2 + \left(U_S + \frac{X_S}{U_S} \cdot \left\{ [(1 - k_{DC})Q_C + Q_L] \left(\frac{U_{PF}}{U_P} \right)^2 + \eta_{RE} k_Q P_{DC} - \frac{\eta_{RE}^2 P_{DC}^2 k_P^2 X_S}{U_S^2} \right\} \right)^2 \right)^{1/2} \quad (12)$$

If takes $A = Q_C(1 - k_{DC}) + Q_L$, $B = \eta_{RE}k_Q P_{DC} - \eta_{RE}^2 P_{DC}^2 k_P^2 X_S U_S^{-2}$, $C = \eta_{RE}^2 k_P^2 P_{DC}^2 X_S U_S^{-1}$, (12) is simplified to:

$$U_{PF}^2 = \left\{ U_S + \frac{X_S}{U_S} \left[A \left(\frac{U_{PF}}{U_P} \right)^2 + B \right] \right\}^2 + C^2 \quad (13)$$

and,

$$\frac{A^2 X_S^2}{U_S^2} \left(\frac{U_{PF}}{U_P} \right)^4 + \left(2AX_S - U_P^2 + 2AB \frac{X_S^2}{U_S^2} \right) \left(\frac{U_{PF}}{U_P} \right)^2 + \left(B^2 \frac{X_S^2}{U_S^2} + 2BX_S U_S^2 + C^2 \right) = 0 \quad (14)$$

Approximately takes $U_P \approx 1$, a quartic equation about U_{PF} can be obtained. For a quartic equation of the form $\alpha U_{PF}^4 + \beta U_{PF}^2 + \gamma = 0$, it can be solved as:

$$U_{PF} = \sqrt{\frac{-\beta \pm \sqrt{\beta^2 - 4\alpha\gamma}}{2\alpha}}, \quad (15)$$

where $\alpha = A^2 X_S^2 U_S^{-2}$, $\beta = 2AX_S + 2AB X_S^2 U_S^{-2} - 1$, $\gamma = B^2 X_S^2 U_S^{-2} + 2BX_S U_S^2 + C^2$.

Substituting α , β , and γ into equation (15), the expression for U_{PF} is derived as (A1) in the Appendix. In (15), the sign of the numerator under the radical should be determined based on the specific context. Generally, $U_{PF} \in (1, 2)$.

Throughout all calculations in this study, it is assumed active and reactive power outputs of the RES comply with equations (5) and (6) during the LVRT process. Regardless of the BB or CF, the TOV of the converter bus after a large DC disturbance can be calculated through the values of k_P , k_Q , and k_{DC} parameters in (12) to (15). Combined with the actual situation, it can be approximately considered when a BB fault occurs in the DC sending end, $k_P \approx 1$, $k_Q \in [-0.3, 0]$; when a CF fault occurs, $k_{DC} \in [0.1, 0.3]$, $k_P \in [0, 1]$, $k_Q \in [0, 0.5]$. To simplify the calculation, the rated transmission capacity of the DC system can be set as the power base value of the calculation process, which is, $P_{DC} = 1$ p.u. The following calculations in this article all use the rated transmission capacity of the DC system as the power base value.

III. SENDING END'S TOV SENSITIVITY ANALYSIS

A. Relationship of Overvoltage and System Impedance

A sensitivity analysis of (A1) is carried out, and the partial derivative can be obtained. Taking the relationship between U_{PF} and X_S as an example:

$$\frac{\partial U_{PF}}{\partial X_S} = \frac{\partial U_{PF}}{\partial \alpha} \frac{\partial \alpha}{\partial X_S} + \frac{\partial U_{PF}}{\partial \beta} \frac{\partial \beta}{\partial X_S} + \frac{\partial U_{PF}}{\partial \gamma} \frac{\partial \gamma}{\partial X_S} \quad (16)$$

The partial derivatives in (16) are shown in appendix (A2)–(A7). Taking CF of the DC system under different impedance X_S as an example, the relationship between the peak voltage of the converter bus and system impedance X_S is analyzed. Considering typical parameters $Q_C + Q_L = 0.4 \sim 0.6$, $\eta_{RE} = 50\%$, $k_{DC} = 0.2$, $k_P = 0.5$, $k_Q = 0.2$, the curve of U_{PF} with X_S is drawn as shown in Fig. 4. It can be clearly seen with the increase of X_S , the TOV shows a nonlinear acceleration increasing trend.

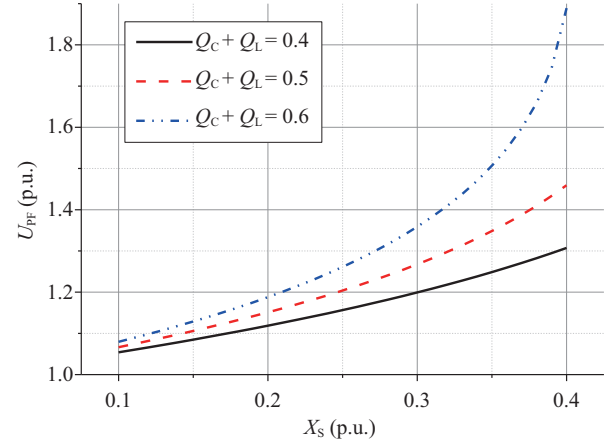


Fig. 4. TOV under different impedance X_S .

B. Relationship between TOV and RES Output Ratio

Different proportions of RES output will affect the TOV of the converter bus. Based on (15) and (A1), taking the CF of the DC system as an example, the typical parameters $X_S = 0.3$, $Q_C + Q_L = 0.4 \sim 0.6$, $k_{DC} = 0.2$, $k_P = 0.5$, $k_Q = 0.2$ are taken to draw the relationship between the converter bus voltage U_{PF} and the RES output ratio η_{RE} , as shown in Fig. 5. It can be seen as η_{RE} increases, the TOV gradually increases, but it shows a nonlinear deceleration growth. At the same time, the reactive power ratio of the filter Q_C has significant impact on the TOV.

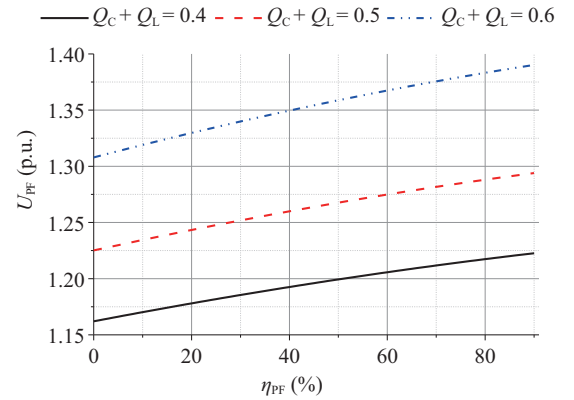


Fig. 5. TOV under different RES output ratios.

C. Relationship of TOV and Active Power Proportion Coefficient of RES During LVRT Process

When CF occurs in the DC's sending end, it may lead the RES to enter the LVRT state first, and then the DC power drops rapidly causing the RES voltage near the DC sending end to rise immediately, while the RES in the LVRT process may also transmit active and reactive power to the grid, further increasing the voltage rise. At present, there is related research on LVRT or high-voltage ride through switching of RES [21], [22]. However, there are few specific quantitative analyses. The existing research shows if the active power ratio of the RES is high during the LVRT process, it will help to reduce the

subsequent voltage rise. This conclusion can be analytically explained by (A1).

Based on (A1), (A8), and (A11), the partial derivative of U_{PF} to k_P can be obtained. Taking the CF fault of DC system as an example, the typical parameters $X_S = 0.3$, $\eta_{RE} = 50\%$, $Q_C + Q_L = 0.5$, $k_{DC} = 0.2$, $k_Q = 0.2$ can be used to write the expression of $\partial U_{PF}/\partial k_P$ under typical working conditions:

$$\frac{\partial U_{PF}}{\partial k_P} \approx 0.001666k_P^3 - 0.044214k_P \quad (17)$$

Through (17), it is clear to see: $\forall k_P \in [0, 1]$, $\partial U_{PF}/\partial k_P \leq 0$. This means the more active power the RES emits during the LVRT process, the lower the TOV during the CF of the converter bus, which helps suppress the TOV. Based on the above typical parameters, the relationship between the peak voltage of the converter bus and the k_P is drawn, as shown in Fig. 6.

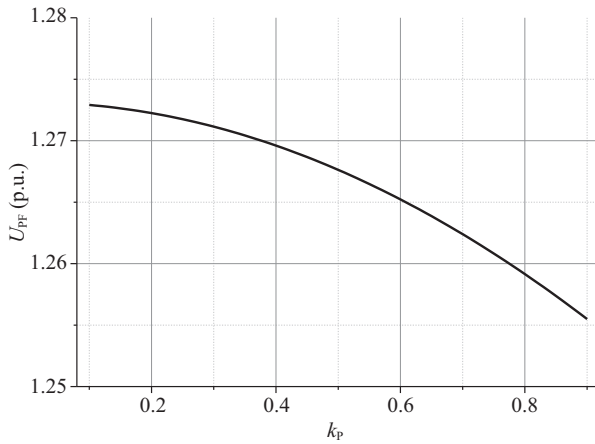


Fig. 6. TOV under different RES LVRT active power coefficient k_P .

D. Relationship of Overvoltage and Reactive Power Proportion Coefficient of RES During LVRT Process

When a CF occurs in the DC system, the voltage of buses near the DC's sending end shows the characteristics of "low first and then high", which is easy to cause RES near the sending end to enter the LVRT, and the voltage is switched from low to high quickly. The RES will still send reactive current in a short time when the converter bus voltage changes from low to high, which further aggravates the voltage rise. According to engineering practice, in order to suppress the TOV after the fault, the reactive current setting value during the LVRT of the RES should be chosen as small as possible [23].

Existing RES, basically, has an LVRT strategy, which is, when the RES detects the grid-connected point voltage is lower than the threshold, RES will increase the reactive current to help lift the system voltage, and decrease the active current to avoid overcurrent of the IGBT. According to the Chinese national standard GB/T 19963.1-2021 *Technical regulations for wind farm access to power system Part 1: Onshore wind power* and GB/T 19964-2012 *Technical regulations for photovoltaic power station access to power system*, when the RES feels the system voltage drop below 0.9 p.u., it should provide dynamic

reactive current. In GB/T 19963.1-2021, the dynamic reactive current ratio coefficient K_1 of a wind farm is stipulated. K_1 should not be less than 1.5, and should not be more than 3 [24]; In GB/T 19964-2012, proportional coefficient of dynamic reactive current is 1.5 [25]. All kinds of national standards describe the reactive power support capacity during the LVRT process through reactive current. However, reactive power is more often used than reactive current. Considering there is usually a long electrical distance between the RES and the converter bus, and the dynamic reactive power support of the RES is quite weak, therefore, the voltage of the RES is usually much lower than 1.0 p.u. during the LVRT process. According to the above, the reactive power coefficient $k_Q \in [0, 1]$ during the LVRT period of RES proposed in this paper is usually 0.05~0.3.

Based on (A1), (A12), and (A15), the partial derivative of U_{PF} to k_Q is obtained. Taking the CF fault of the DC system as an example, the typical parameters $X_S = 0.3$, $\eta_{RE} = 50\%$, $Q_C + Q_L = 0.5$, $k_{DC} = 0.2$, $k_P = 0.5$, can be used to write the expression of $\partial U_{PF}/\partial k_Q$ under typical working conditions:

$$\frac{\partial U_{PF}}{\partial k_Q} \approx 0.000829k_Q^2 + 0.02652k_Q + 0.23588 \quad (18)$$

Through (18), it can be seen: $\forall k_Q \in [0, 1]$, $\partial U_{PF}/\partial k_Q > 0$. This means the dynamic reactive current emitted by the RES during the LVRT process will increase the TOV during CF. In practical engineering and operation, under the premise of ensuring various security and stability constraints, smaller k_Q and K_1 values should be selected to minimize the TOV during CF.

Based on the above typical parameters, the relationship between converter bus voltage U_{PF} and k_Q is drawn, as shown in Fig. 7.

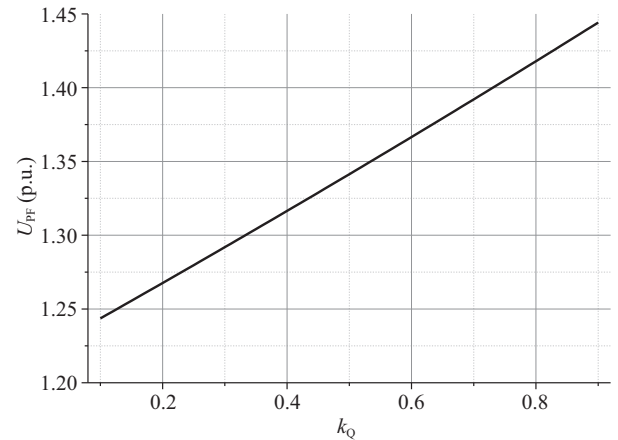


Fig. 7. TOV under different new energy LVRT reactive power coefficient k_Q .

E. Evaluation Method of TOV and η_{re} and SCR

The proportion of RES output, DC's SCR, and system TOV level are three indicators more concerned in the field of power grid planning. Many literature studies have shown large-scale access to RES will affect the system's SCR and TOV. Equations (14) and (A1) are based on the typical sending-end

grid topology, and the analytical relationship between the three is listed. If the sending end DC's SCR k_{SCR} is considered as:

$$k_{SCR} = \frac{S_{SC}}{P_{DC}} \approx X_S^{-1} \quad (19)$$

The calculation formula of system TOV based on the SCR can be obtained. Bringing (18) into (13), we can calculate the minimum SCR corresponding to different RES output ratios when the TOV level does not exceed the limit, or the maximum RES output ratio under different SCR.

Considering U_{PF-BB} as the TOV of the converter bus under the BB fault, and U_{PF-CF} as the TOV of the converter bus under the CF fault, taking the typical parameters of the BB and the CF fault as examples, the renewable energy output ratio η_{RE} , k_{SCR} , and TOV curves under different DC faults are drawn, as shown in Figs. 8 and 9. Typical system parameters of BB are $Q_C + Q_L = 0.5$, $k_{DC} = 0$, $k_P = 1$, $k_Q = 0$, and for CF are $Q_C + Q_L = 0.5$, $k_{DC} = 0.2$, $k_P = 0.5$, $k_Q = 0.2$.

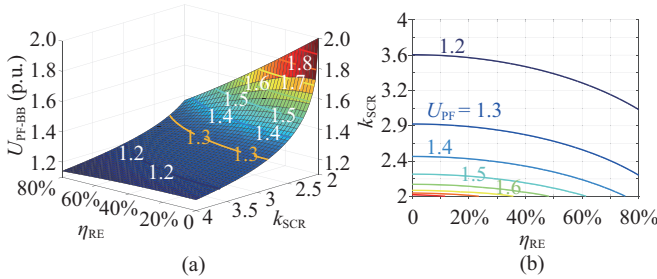


Fig. 8. TOV after BB with different η_{RE} and SCR. (a) Overvoltage distribution. (b) Projection figure.

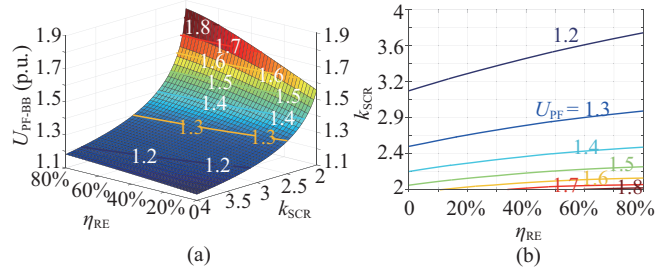


Fig. 9. TOV after CF with different η_{RE} and SCR. (a) Overvoltage distribution. (b) Projection figure.

Figures 8 and 9 show the TOV situation after BB and CF, but the evolution trend of the two is obviously different.

Two types of faults occur in the DC system. Under a certain k_{SCR} , the TOV does not show the same trend as the proportion of RES output. Under the BB fault, because the active power of the RES remains similar to before the fault, the effect of reducing the converter bus voltage is more significant, resulting in a higher proportion of RES output under the BB fault and a lower TOV. For the CF fault, although the RES still emits some active power after the fault, it will also emit dynamic reactive power. The voltage-reactive power sensitivity is significantly greater than the voltage-active power sensitivity. Even if the RES emits a small amount of reactive power, the converter bus voltage is significantly increased.

Therefore, the TOV caused by the CF fault will increase with the increase of η_{RE} .

Critical voltage of the converter bus $U_{PF-CF} = 1.3$ p.u. is usually used as a key indicator to measure the TOV [24], [25]. The contour line with a voltage of 1.3 can be used as the limiting condition in Figs. 8 and 9. When the voltage in Figs. 8(b) and 9(b) is 1.3, the boundary relationship between η_{RE} and the DC's SCR under TOV constraints can be described.

Further analysis is carried out to compare the difference in TOV distribution under two types of DC faults. Figs. 8(a) and 9(a) are drawn together in Fig. 10(a). The red curve in Fig. 10(a) is the intersection of two surfaces, that is, $U_{PF-BB} = U_{PF-CF}$. On the basis of Fig. 10(a), the projection diagram of the difference between the two types of TOV values under different η_{RE} and SCR is drawn, as shown in Fig. 10(b).

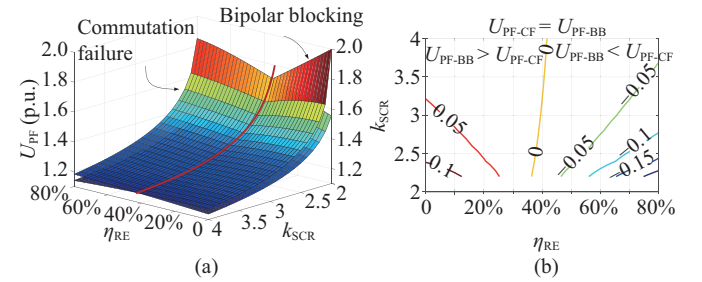


Fig. 10. TOV two types of DC faults with different η_{RE} and SCR. (a) Overvoltage distribution. (b) Projection figure.

Figure 10(b) is the projection of Fig. 10(a) to the bottom. The curve with the yellow value of 0 in the middle of Fig. 10(b) is the red intersection line in Fig. 10(a), which represents the two types of DC fault TOV are equal. In Fig. 10(b), the left side of the curve with a value of 0 represents $U_{PF-BB} > U_{PF-CF}$, that is, the TOV caused by BB fault is more serious; the right side of the curve represents $U_{PF-BB} < U_{PF-CF}$, indicating CF causes more serious TOV.

Combined with Figs. 8(b), 9(b), and 10(b), the relationship between η_{RE} and k_{SCR} under different TOV constraints can be drawn after two types of DC faults under typical parameters, as shown in Fig. 11.

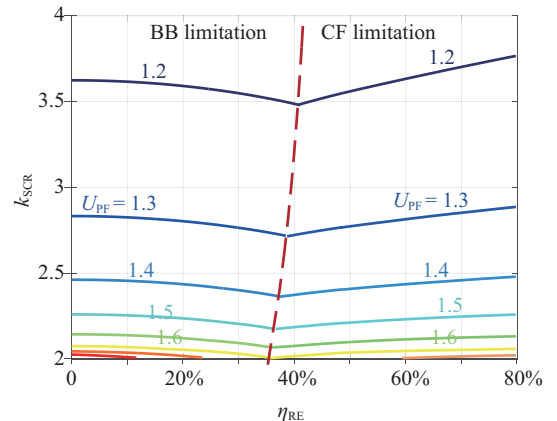


Fig. 11. Relation between output ratio and SCR under different overvoltage constraints for two types of DC faults.

In Fig. 11, the left side is the limitation of BB, and the right side is the limitation of CF. In engineering applications, based on the actual system parameters, the relationship between η_{RE} and k_{SCR} is constructed as shown in Fig. 11, and the system conditions under different TOV constraints are determined according to the above figures.

IV. CASE STUDY OF SENDING END'S TOV

A. Analysis of the Influence of η_{RE}

Using the system illustrated in Fig. 2 as a reference, we construct a simplified model based on a ± 800 kV UHVDC transmission system.

To accommodate RES output while maintaining constant DC transmission power, two common methods are typically employed: decreasing the starting or output of synchronous machines. The following two methods are used to explore the TOV under different working conditions.

Reducing the output of the synchronous machine to accept RES, the active output is reduced while keeping the synchronous generator start-up. As a result, under different η_{RE} , the k_{SCR} of the converter bus remains almost unchanged, but the TOV changes significantly. Assuming k_P maintains 1, the relevant results and the waveforms are shown in Table I and Fig. 12.

When analyzing the TOV of the converter bus by reducing the startup of synchronous machines to accept RESs, this

TABLE I
TOV RESULTS OF DIFFERENT METHODS FOR BB UNDER DIFFERENT η_{RE} (%) WITH REDUCING THE OUTPUT METHOD

Parameters	$\eta_{RE} = 0\%$	$\eta_{RE} = 25\%$	$\eta_{RE} = 50\%$	$\eta_{RE} = 75\%$
k_{SCR}	3.5323	3.5323	3.5323	3.5322
U_{P0} (p.u.)	1.002	1.002	1.003	1.004
U_{PF} of PSD (p.u.)	1.2449	1.2032	1.1813	1.1733
U_{PF} of (1) [9] (p.u.)	1.1415	1.1415	1.1415	1.1415
Error between PSD and U_{PF} of (1) (%)	-8.31	-5.13	-3.37	-2.71
U_{PF} of (2) [13] (p.u.)	1.2056	1.2057	1.2057	1.2057
Error between PSD and U_{PF} of (2) (%)	-3.16	0.21	2.07	2.76
U_{PF} of (21) (p.u.)	1.2048	1.2004	1.1857	1.1666
Error between PSD and U_{PF} of (21) (%)	-3.14	-0.15	0.63	-0.23

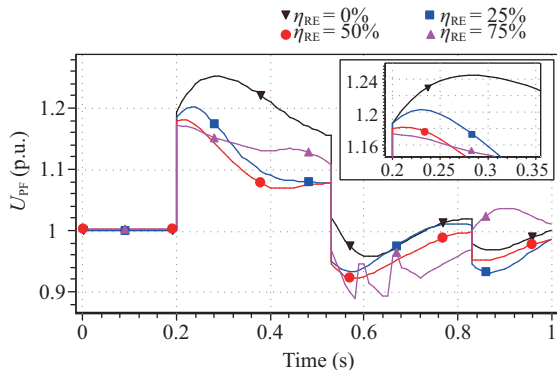


Fig. 12. Converter bus voltage after BB under different η_{RE} with reducing the output method.

can be achieved by adjusting the synchronous machine power supply and the capacity of RES grid-connected units. When the fully synchronous machine is connected, the SCR of the converter bus is 3.5323 as the benchmark for subsequent analysis. Assuming $k_P = 1$, the analysis methods of (1) from [9] and (2) from [13] are compared with results of PSD-ST power system simulation software. The calculation results and simulation waveforms are shown in Table II and Fig. 13.

TABLE II
TOV RESULTS OF DIFFERENT METHODS FOR BB UNDER DIFFERENT η_{RE} (%) WITH REDUCING THE START-UP METHOD

Parameters	$\eta_{RE} = 0\%$	$\eta_{RE} = 25\%$	$\eta_{RE} = 50\%$	$\eta_{RE} = 75\%$
k_{SCR}	3.5323	3.0966	2.6332	2.1289
U_{P0} (p.u.)	1.002	1.002	1.000	0.998
U_{PF} of PSD (p.u.)	1.2449	1.2582	1.2781	1.3259
U_{PF} of (1) [9] (p.u.)	1.1415	1.1615	1.1899	1.2349
Error between PSD and U_{PF} of (1) (%)	-8.31	-7.69	-6.90	-6.86
U_{PF} of (2) [13] (p.u.)	1.2058	1.2539	1.342	1.6051
Error between PSD and U_{PF} of (2) (%)	-3.14	-0.34	5.00	21.06
U_{PF} of (21) (p.u.)	1.2058	1.2473	1.2977	1.3517
Error between PSD and U_{PF} of (21) (%)	-3.06	-0.79	1.53	1.79

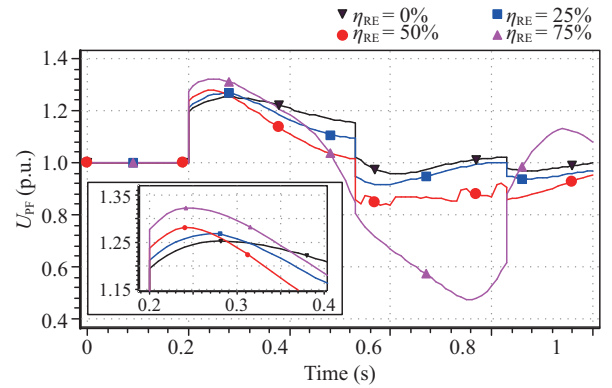


Fig. 13. Converter bus voltage after BB under different η_{RE} with reducing the start-up method.

Different ways of accepting RES will produce different TOV results. When the RES is accepted in the way of reducing the output of synchronous generators, the TOV will increase with decrease of η_{RE} . However, the TOV increases with the increase of η_{RE} when the RES is accepted in the way of reducing the start-up of synchronous generators.

Under a typical system as shown in Fig. 2, the methods proposed in [9] and [13] have certain errors, since there is only one equivalent power source in their model by combining RES and synchronous generators together. Ignorance of RES induces the calculation error.

Equation (15) takes into account the impact of RES on the TOV of the converter bus, thereby obtaining higher-precision calculation results.

Taking the system shown in Fig. 2 as an example as well, when the CF occurs in the DC system with different η_{RE} , the calculation method proposed in [16] is compared with the calculation method proposed in this paper. According to

TABLE III
RESULTS OF VARIOUS METHODS FOR CF UNDER DIFFERENT η_{RE} (%)

Parameters	$\eta_{RE} = 0\%$	$\eta_{RE} = 25\%$	$\eta_{RE} = 50\%$	$\eta_{RE} = 75\%$
k_{SCR}	3.5323	3.0966	2.6332	2.1289
U_{P0} (p.u.)	1.002	1.002	1.000	0.998
U_{PF} of PSD (p.u.)	1.2544	1.2831	1.3352	1.4828
U_{PF} of (3) [16] (p.u.)	1.1632	1.2004	1.2667	1.4401
Error between PSD and U_{PF} of (3) (%)	-7.27	-6.45	-5.13	-2.88
U_{PF} of (21) (p.u.)	1.2255	1.2767	1.3204	1.4831
Error between PSD and U_{PF} of (21) (%)	-2.23%	-0.42%	-1.11%	-0.11%

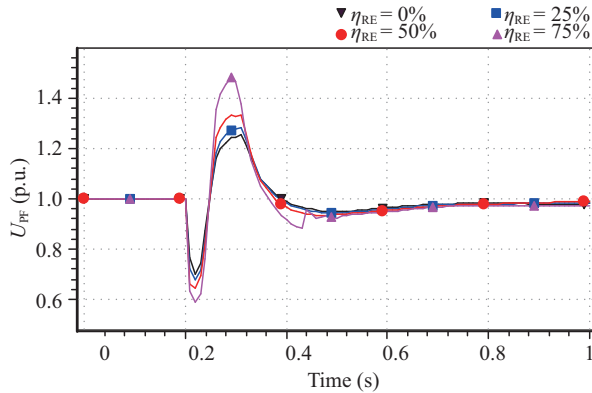


Fig. 14. The waveforms of the converter bus after CF under different η_{RE} .

the actual engineering data, set $k_P = 0.5$, $k_Q = 0.1$, $k_{DC} = 0.2$, and accept RES access by reducing start-up method, the calculation results and simulation waveforms are shown in are shown in Table III and Fig. 14.

Through Table III and Fig. 14, it can be observed, with the increase in the proportion of η_{RE} , the TOV at the converter bus following commutation failure, gradually decreases. Comparing the method proposed in [16] with that in this paper, it can be seen under the same calculation parameters, this paper obtains better calculation accuracy by considering the influence of active and reactive power on the TOV in the process of the DC fault of the RES.

B. The Influence of Different Parameters During LVRT Process on TOV

Taking the system shown in Fig. 4 as an example, under the typical parameters of the DC system, the influence of different active parameters during LVRT on the system TOV is obtained by changing the active power coefficient k_P of the RES during the LVRT. $k_{SCR} = 2.1289$, $\eta_{RE} = 75\%$, $k_Q = 0.1$, and the SCR is summarized in Table IV and Fig. 15.

Taking the system shown in Fig. 4 as an example, under the typical parameters of the DC system, the influence of different LVRT reactive power parameters on the system TOV is obtained by changing the reactive power coefficient k_Q during the LVRT of the RES. It is summarized in Table V and Fig. 16.

As the theoretical analysis results of (17) and (18), the different parameters of RES during the LVRT will affect the TOV of the converter bus. At the same time, the theoretical calculation results are close to the simulation values.

TABLE IV
RESULTS OF VARIOUS METHODS FOR CF UNDER DIFFERENT k_P

k_P	PSD Result (p.u.)	U_{PF} of (21) (p.u.)
0.2	1.5207	1.5423
0.5	1.4819	1.4831
0.8	1.4451	1.4032

TABLE V
COMPARISON OF RESULTS OF VARIOUS METHODS FOR CF UNDER DIFFERENT REACTIVE POWER COEFFICIENT k_Q

K_1	k_Q	PSD Result (p.u.)	U_{PF} of (21) (p.u.)
0.5	0.08	1.4818	1.4829
1.5	0.1	1.4819	1.4831
3	0.15	1.4923	1.5369

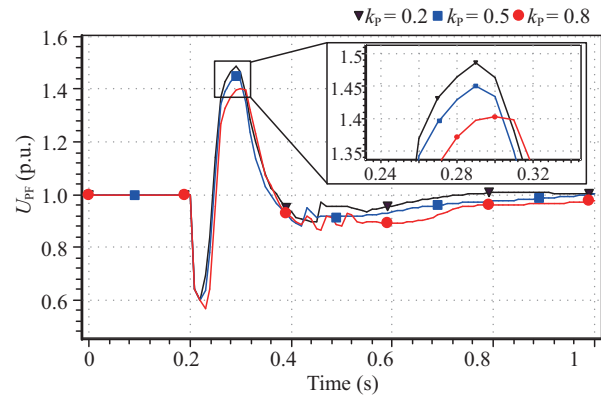


Fig. 15. Converter bus voltage after commutation failure under different active power coefficient k_P .

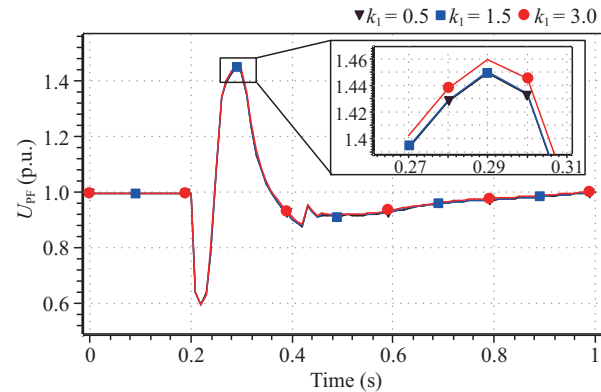


Fig. 16. Voltage of commutating bus after commutation failure under different reactive power coefficient k_Q .

C. Analysis of Actual Power Grid

Based on regional grid integration of RES in China, an individual evaluation of RESs, synchronous generators and grid power flow is carried out. Additionally, AC filter and SCR of each DC are considered. Besides, it is necessary to conduct equivalent statistics on the control parameters during the LVRT period of RES in the area near the DC sending end. Fig. 17 shows the grid connection diagram.

Although there are several DC systems in the system shown in Fig. 17, there exists a certain electrical distance between each DC converter bus. Considering reactive power cannot be transmitted over long distances; it can be approximated

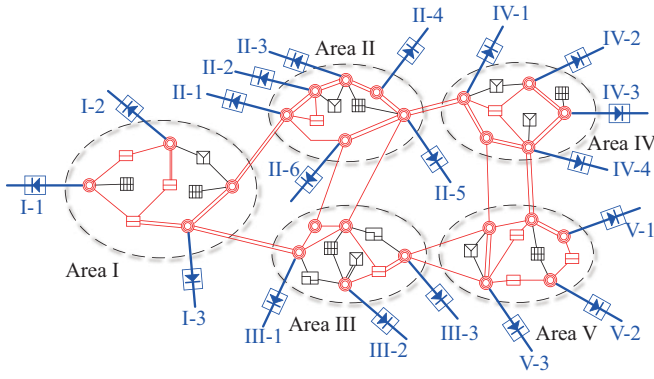


Fig. 17. Diagram of DC transmission of a power grid.

there is no mutual influence of the DC systems when a single fault occurs in one of the DC system. The system shown in Fig. 2 can be used to analyze the TOV in the system shown in Fig. 17 after two types of faults occur in each DC system converter bus. The corresponding TOV calculation results are obtained by PSD-ST software. The LVRT parameters of each DC systems corresponding to the RES are different. For BB, parameters can take $k_P = 1$, $k_Q = 0$, $k_{DC} = 0$, and for CF, $k_P = 0.2 \sim 0.8$, $k_Q = 0.1 \sim 0.3$, $k_{DC} = 0.2$. Table VI shows the comparison of TOV between the PSD-ST's simulation, and U_{PF} by (21), results calculated in this paper.

In Table VI, the simulated values of TOV at each DC converter bus under two types of faults are very close to the calculated values obtained through (21), and the error is generally not more than 5%. It can be seen the method proposed in this paper has good engineering application value.

From the error level analysis, the results of the calculation method proposed in this paper are close to the simulation values under the BB fault. The error is mainly caused by the approximate equivalence of each RES and the neglect of the excitation part of the synchronous generators. Meanwhile, the error under the CF fault is generally greater than under

the BB fault. This is mainly since this paper believes that during the CF, the RES is transmitted according to the low wear active and reactive power coefficients to constant power, ignoring other dynamic characteristics. As the η_{RE} increases, the calculation error also increases. On the whole, under the two types of faults, the error between the simulation value and the calculated value is basically within $\pm 5\%$, which can meet the needs of engineering calculation.

D. Application of Overvoltage Evaluation Method in Actual Grid Planning

Taking DC system III-1 as an example, the characteristics of TOV and corresponding optimization measures are analyzed in detail, combined with the evaluation method of the relationship between TOV, η_{RE} , and SCR.

For the DC system III-1, although its reactive power $Q_C + Q_L$ is the smallest among all the DC systems, the η_{RE} is not the highest, due to its long electrical distance from the main network and less local synchronous sources, the DC system III-1 has the weakest support, and the TOV after DC fault is significantly higher than other DC systems.

Based on the specific parameters of the DC system III-1, combined with section 3.5 evaluation method, the relationship diagram under the CF fault can be drawn, as shown in Fig. 18. Taking the analysis result shown in Fig. 18 as an example, the relationship between η_{RE} , k_{SCR} and TOV with and without the optimization measures are clearly compared. When no adjustment measures are used, the TOV after CF is 1.442 p.u.

Considering, the TOV is mainly influenced by η_{RE} , k_{SCR} and parameters of RES during LVRT, optimizing methods can be taken as following as an example.

- Reduce the delivery power of DC system.
- Reduce the η_{RE} of near-field of DC system.
- Optimize the start-up of synchronous generators.
- Add synchronous condensers (SC).
- Optimize the parameters of RES during LVRT.

TABLE VI
DC PARAMETERS AND TOV AFTER TWO KINDS OF DC FAULTS

DC Symbol	k_{SCR}^*	$Q_C + Q_L$ (p.u.)	η_{RE} (%)	U_{P0} (p.u.)	Bipolar Blocking			Commutation Failure		
					PSD (p.u.)	U_{PF} (p.u.)	Error (%)	PSD (p.u.)	U_{PF} (p.u.)	Error (%)
I-1	4.674	0.618	30	1.004	1.186	1.174	-3.41	1.201	1.178	-3.13
I-2	5.196	0.726	0	0.991	1.124	1.139	1.35	1.144	1.102	-3.62
I-3	4.255	0.553	50	1.037	1.215	1.222	3.06	1.217	1.202	0.06
II-1	4.097	0.636	90	0.998	1.153	1.166	1.13	1.152	1.184	2.90
II-2	3.020	0.642	95	1.005	1.218	1.223	0.34	1.253	1.247	-0.37
II-3	3.167	0.679	95	0.999	1.163	1.213	4.26	1.223	1.231	0.83
II-4	3.182	0.651	95	0.995	1.174	1.213	3.31	1.219	1.231	1.17
II-5	4.358	0.706	52	0.994	1.124	1.138	1.27	1.108	1.136	2.64
II-6	3.192	0.684	95	0.999	1.160	1.198	3.26	1.242	1.244	0.52
III-1	2.145	0.492	80	0.987	1.278	1.308	2.36	1.486	1.501	1.66
III-2	5.524	0.493	95	0.994	1.103	1.114	0.99	1.178	1.150	-2.22
III-3	3.059	0.633	90	0.997	1.254	1.277	1.80	1.338	1.348	1.33
IV-1	3.440	0.612	13	1.001	1.228	1.300	5.86	1.203	1.249	3.82
IV-2	4.643	0.508	10	1.012	1.191	1.177	-1.19	1.167	1.154	-1.11
IV-3	3.790	0.569	10	1.001	1.298	1.286	-0.93	1.249	1.249	0.02
IV-4	4.918	0.542	10	1.000	1.148	1.167	1.66	1.147	1.144	-0.35
V-1	4.812	0.652	0	1.001	1.189	1.193	0.35	1.144	1.153	0.80
V-2	5.117	0.629	0	1.007	1.179	1.168	-0.95	1.170	1.133	-3.15
V-3	4.870	0.729	90	1.004	1.154	1.172	1.56	1.154	1.168	1.29

* k_{SCR} is calculated based on the results of the power flow.

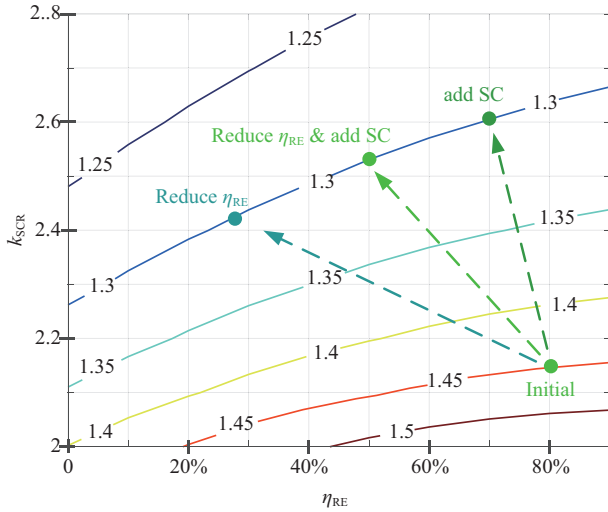


Fig. 18. Relationship of η_{RE} , k_{SCR} and TOV of DC III-1 after CF.

For DC system III-1, some measures are taken to suppress the TOV of the converter bus. The TOV of DC system III-1 can be effectively reduced to below 1.3 p.u. by reducing η_{RE} from 80% to 28%, or adding seven 300 Mvar synchronous condensers, or reducing the η_{RE} from 80% to 45% by reducing the output of synchronous generators and adding four 300 Mvar SC.

V. CONCLUSION

Considering the influence of RES access on the TOV caused by BB and CF in the DC system, the quantitative methods for TOV are proposed respectively, and a unified equation suitable for the two types of faults is formed.

The TOV caused by the DC system fault in the sending end power grid is closely related to the large-scale access of RES. Through sensitivity analysis, the influence of the proportion of RES output, active power coefficient, and reactive power coefficient during the LVRT process of RES on the TOV after the DC fault is revealed. TOV increases with the increase of the proportion of renewable energy output, and it is approximately linear with the active power coefficient and reactive power coefficient during the LVRT process of RES.

Taking typical system parameters as an example, the influence of the RES output ratio and SCR on post-fault TOV under different DC faults is analyzed. Based on the typical system parameters, the constraint relationship between TOV, renewable energy output ratio and SCR is constructed. Based on the typical system at the sending end and the actual large-scale DC transmission system, correctness and practicability of the calculation method proposed in this paper are verified, and the solution to optimize the TOV is proposed in combination with the actual system.

APPENDIX

$$U_{PF} = \frac{U_P}{\sqrt{2}(1 - k_{DC})Q_C X_S} \left\{ [U_P^2 U_S^2 - 2[(1 - k_{DC})Q_C + Q_L]P_{DC}Q_C X_S^2 (k_Q \eta_{RE} - P_{DC} X_S k_P^2 \eta_{RE}^2 U_S^{-2}) - 2[(1 - k_{DC})Q_C + Q_L]U_S^2 X_S] \right.$$

$$\left. + \sqrt{4[(1 - k_{DC})Q_C + Q_L]P_{DC}^2 X_S^3 k_P^2 \eta_{RE}^2 (U_P^2 - A X_S) - 4[(1 - k_{DC})Q_C + Q_L]U_P^2 U_S^2 X_S} \right\}^{1/2} \quad (A1)$$

$$\frac{\partial U_{PF}}{\partial \alpha} = \frac{\beta \mp \sqrt{\beta^2 - 4\alpha\gamma}}{2\alpha^2} \mp \frac{\gamma}{\alpha \sqrt{\beta^2 - 4\alpha\gamma}} \quad (A2)$$

$$\frac{\partial U_{PF}}{\partial \beta} = \frac{-1 \pm \frac{\beta}{\sqrt{\beta^2 - 4\alpha\gamma}}}{4\alpha \sqrt{\beta^2 - 4\alpha\gamma}} \quad (A3)$$

$$\frac{\partial U_{PF}}{\partial \gamma} = -\frac{1}{2\sqrt{\beta^2 - 4\alpha\gamma} \sqrt{-\frac{\beta \mp \sqrt{\beta^2 - 4\alpha\gamma}}{2\alpha}}} \quad (A4)$$

$$\frac{\partial \alpha}{\partial X_S} = \frac{2X_S}{U_S} [(1 - k_{DC})Q_C + Q_L]^2 \quad (A5)$$

$$\frac{\partial \beta}{\partial X_S} = 2[(1 - k_{DC})Q_C + Q_L] \cdot \left[1 + \frac{2X_S k_Q \eta_{RE}}{U_S^2} - \frac{3X_S^2 k_P^2 \eta_{RE}^2}{U_S^4} \right] \quad (A6)$$

$$\frac{\partial \gamma}{\partial X_S} = 2 \left(k_Q \eta_{RE} - \frac{X_S \eta_{RE}^2 k_P^2}{U_S^2} \right) \left(\frac{X_S}{U_S^2} k_Q \eta_{RE} - \frac{2X_S^2 \eta_{RE}^2 k_P^2}{U_S^4} \right) - \frac{2X_S \eta_{RE}^2 k_P^2}{U_S^2} + 2k_Q \eta_{RE} \quad (A7)$$

$$\frac{\partial U_{PF}}{\partial k_P} = \frac{\partial U_{PF}}{\partial \alpha} \frac{\partial \alpha}{\partial k_P} + \frac{\partial U_{PF}}{\partial \beta} \frac{\partial \beta}{\partial k_P} + \frac{\partial U_{PF}}{\partial \gamma} \frac{\partial \gamma}{\partial k_P} \quad (A8)$$

$$\frac{\partial \alpha}{\partial k_P} = 0 \quad (A9)$$

$$\frac{\partial \beta}{\partial k_P} = -4[(1 - k_{DC})Q_C + Q_L] \frac{X_S^3 k_P \eta_{RE}^2}{U_S^4} \quad (A10)$$

$$\frac{\partial \gamma}{\partial k_P} = -\frac{2X_S^2 k_P \eta_{RE}^2}{U_S^2} - \frac{4X_S^3 k_P \eta_{RE}^2}{U_S^4} \left(k_Q \eta_{RE} - \frac{X_S \eta_{RE}^2 k_P^2}{U_S^2} \right) \quad (A11)$$

$$\frac{\partial U_{PF}}{\partial k_Q} = \frac{\partial U_{PF}}{\partial \alpha} \frac{\partial \alpha}{\partial k_Q} + \frac{\partial U_{PF}}{\partial \beta} \frac{\partial \beta}{\partial k_Q} + \frac{\partial U_{PF}}{\partial \gamma} \frac{\partial \gamma}{\partial k_Q} \quad (A12)$$

$$\frac{\partial \alpha}{\partial k_Q} = 0 \quad (A13)$$

$$\frac{\partial \beta}{\partial k_Q} = 2 \frac{X_S^2 \eta_{RE}}{U_S^2} [(1 - k_{DC})Q_C + Q_L] \quad (A14)$$

$$\frac{\partial \gamma}{\partial k_Q} = 2X_S \eta_{RE} + 2 \frac{X_S^2 \eta_{RE}}{U_S^2} \left(k_Q \eta_{RE} - \frac{X_S \eta_{RE}^2 k_P^2}{U_S^2} \right) \quad (A15)$$

REFERENCES

- [1] B. A. Xin, M. Chen, P. Zhao, H. D. Sun, Q. Y. Zhou, and X. H. Qin, "Research on coal power generation reduction path considering power supply adequacy constraints under carbon neutrality target in China," *Proceedings of the CSEE*, vol. 42, no. 19, pp. 6919–6930, Oct. 2022.
- [2] X. X. Zhou, S. Y. Chen, Z. X. Lu, Y. H. Huang, S. C. Ma, and Q. Zhao, "Technology features of the new generation power system in China," *Proceedings of the CSEE*, vol. 38, no. 7, pp. 1893–1904, Apr. 2018.
- [3] Y. B. Shu, Z. G. Zhang, J. B. Guo, and Z. L. Zhang, "Study on key factors and solution of renewable energy accommodation," *Proceedings of the CSEE*, vol. 37, no. 1, pp. 1–8, Jan. 2017.
- [4] W. L. Zhang, X. X. Zhou, J. B. Guo, Y. H. Yin, Y. Tang, and Q. Guo, "Feasibility of ± 1000 kV Ultra HVDC in the power grid of China," *Proceedings of the CSEE*, vol. 27, no. 28, pp. 1–5, Oct. 2007.
- [5] J. B. Guo, T. Z. Wang, K. Luo, X. H. Qin, Y. R. Jing, B. Zhao, and S. C. Ma, "Development of new power systems: challenges and solutions," *New Type Power Systems*, vol. 1, no. 1, pp. 32–43, Jun. 2023.

- [6] W. S. Wang, G. H. Li, and J. B. Guo, "Large-scale renewable energy transmission by HVDC: challenges and proposals," *Engineering*, vol. 19, pp. 252–267, Dec. 2022.
- [7] *Code on Security and Stability for Power System*, GB 38755–2019, 2019.
- [8] L. Yu, H. D. Sun, S. Y. Xu, B. Zhao, and J. Zhang, "A critical system strength evaluation of a power system with high penetration of renewable energy generations," *CSEE Journal of Power and Energy Systems*, vol. 8, no. 3, pp. 710–720, May 2022.
- [9] J. B. He, W. Zhuang, T. Xu, C. Huo, and W. Y. Jiang, "Study on cascading tripping risk of wind turbines caused by transient overvoltage and its countermeasures," *Power System Technology*, vol. 40, no. 6, pp. 1844–1849, Jun. 2016.
- [10] P. P. Han, L. Q. Chen, D. Hu, and Y. Zhang, "Impact of transient overvoltage caused by DC block on wind power transmission and its suppression measure," *Power System Protection and Control*, vol. 46, no. 5, pp. 99–105, Mar. 2018.
- [11] J. Z. Tu, J. Zhang, G. Q. Bu, J. Yi, Y. H. Yin, and J. C. Jia, "Analysis of the sending-side system instability caused by multiple HVDC commutation failure," *CSEE Journal of Power and Energy Systems*, vol. 1, no. 4, pp. 37–44, Dec. 2015.
- [12] Q. Y. Zhou, Y. T. Zhang, Z. X. Liu, L. Yun, and H. B. Shi, "Research on technical requirement of DC rectifier station determined by transient voltage constraint," *High Voltage Engineering*, vol. 46, no. 6, pp. 2057–2063, Jun. 2020.
- [13] X. Y. Li, F. T. Li, C. Y. Yin, and H. B. Bai, "Transient overvoltage calculation method of HVDC sending-end system under DC bipolar blocking," *Power System Protection and Control*, vol. 49, no. 1, pp. 1–8, Jan. 2021.
- [14] F. Wang, T. Q. Liu, Y. Y. Ding, Q. Zeng, and X. Y. Li, "Calculation method and influencing factors of transient overvoltage caused by HVDC block," *Power System Technology*, vol. 40, no. 10, pp. 3059–3065, Oct. 2016.
- [15] G. Q. He, W. S. Wang, C. Liu, G. H. Li, and H. Nian, "Commutation failure of UHVDC system for wind farm integration (part I): transient reactive power and voltage modeling of wind Powers in sending terminal grid," *Proceedings of the CSEE*, vol. 42, no. 12, pp. 4391–4404, Jun. 2022.
- [16] J. H. Sun, X. X. Wang, G. H. Li, and X. Zhang, "Quantitative calculation and influencing factors of overvoltage of sending-side system caused by commutation failure," *Proceedings of the CSU-EPSA*, vol. 32, no. 12, pp. 62–68, Dec. 2020.
- [17] A. C. Xue, L. Yue, J. H. Zhang, J. H. Cui, Z. Q. Li, Y. C. Li, L. Gao, W. F. Lin, and X. Y. Ren, "A new quantitative analysis method for overvoltage in sending end electric power system with UHVDC," *IEEE Access*, vol. 8, pp. 145898–145908, Aug. 2020.
- [18] Y. L. Wang, L. Zou, Y. S. Chen, and S. W. Fang, "Research on overvoltage and fault of a UHV AC/DC hybrid system," *The Journal of Engineering*, vol. 2019, no. 16, pp. 2106–2111, Mar. 2019.
- [19] C. Y. Yin and F. T. Li, "Analytical expression on transient overvoltage peak value of converter bus caused by DC faults," *IEEE Transactions on Power Systems*, vol. 36, no. 3, pp. 2741–2744, May 2021.
- [20] J. Z. Tu, J. Zhang, M. S. Liu, Y. Pan, G. W. Xi, and J. Yi, "Mechanism analysis of transient overvoltage with large disturbance considering dynamic characteristics of wind generator," *Automation of Electric Power Systems*, vol. 44, no. 11, pp. 197–205, Jun. 2020.
- [21] X. C. Wang, C. Liu, W. F. Lin, and H. B. Xie, "Influence of wind turbine fault ride-through characteristics on transient overvoltage of large-scale wind power DC transmission systems and parameter optimization," *Power System Technology*, vol. 45, no. 12, pp. 4612–4620, Dec. 2021.
- [22] Y. K. Zhou, H. Xie, H. D. Sun, S. Y. Xu, B. Zhao, Y. Zhang, X. Q. Chang, and J. Zhang, "Influence of renewable energy low voltage ride-through control parameters on overvoltage," *Power System Technology*, vol. 46, no. 5, pp. 1907–1916, May 2022.
- [23] J. C. Jia, Y. D. Jin, B. Zhao, W. Z. Zhong, S. G. Cheng, T. Liu, X. W. Xu, and S. F. Zheng, "Impact analysis and performance optimization of LVRT control of wind turbine on transient overvoltage of power system," *Power System Technology*, vol. 45, no. 2, pp. 526–533, Feb. 2021.
- [24] *Technical Specification for Connecting Wind Farm to Power System—Part 1: On Shore Wind Power*, GB/T 19963.1-2021, 2021.
- [25] *Technical Requirements for Connecting Photovoltaic Power Station to Power System*, GB/T 19964-2012, 2012.



Jianbo Guo received the B.S. degree from the Huazhong University of Science and Technology, Wuhan, China, in 1982 and the M.S. degree from China Electric Power Research Institute, Beijing, China, in 1984. From 2010 to 2019, he was the Chairman of China Electric Power Research Institute, Beijing, China. Since 2013, he has been an Elected Academician of the Chinese Academy of Engineering, Beijing, China. He is currently the Deputy Chief Engineer of State Grid Corporation of China, Beijing, China, Vice Chairman of Chinese Society for Electrical Engineering, and honorary Chairman of China Electric Power Research Institute, Beijing, China. He has been dedicated to the clean use of energy and the development of environmentally friendly power grid. He has long engaged in power system analysis and control. He has made remarkable achievements in power grid planning, improving security, reliability and transfer capability of power grid, and security of wind power integration. As the Principal Investigator, he participated in Chinese National Programs for Three Gorges Power Transmission Project and many other important grid planning studies. He presided over the development plan for Chinese National Grid Interconnection Project (from 2020 to 2050). He successfully developed Thyristor Controlled Series Compensation and UHV series compensator (1000kV) with proprietary IPR. Prof. Guo was the recipient of the first and second prizes of the National Science and Technology Progress Award in 2008 and 2015, the Ho Leung Ho Lee Foundation Science and Technology Progress Award in 2011 and FEIAP Engineer of the Year Award 2018.



Qiang Guo received a Ph.D degree in Electrical Engineering from Xi'an Jiaotong University, Xi'an, China, in 1998. He is currently the Vice Director of the China Electric Power Research Institute (CEPRI) and a Professorate Senior Engineer. His main research interests include power system planning, operations and control.



Jian Zhang received the Ph.D. degree in Electrical Engineering from the China Electric Power Research Institute (CEPRI), Beijing, China, in 2015. He is currently the Director of the Power System Planning Technology Division, Power System Department, CEPRI, where he is also a Professorate Senior Engineer. His research interests include power system analysis and power system operation and control.



Qinyong Zhou received the Ph.D. degree in Electrical Engineering from Shandong University, Jinan, China, in 2015. He is currently the Deputy Director of the Power System Department, China Electric Power Research Institute (CEPRI). He is also a Professorate Senior Engineer. His main research interests include power system planning and operation, power system transient stability, and new technology applications.



Libo Zhang received the Ph.D. degree in Electrical Engineering from Shanghai Jiao Tong University, Shanghai, China. He is currently the vice Director of the Power System Planning Technology Division, Power System Department, CEPRI, where he is also a Senior Engineer. His research interests include power system analysis, power system planning and power system operation and control.



Haoyue Gong received the B.S. degree in Electrical Engineering from Beijing Jiao Tong University, Beijing, China, in 2018. He is currently working toward the Ph.D. degree in Electrical Engineering at China Electric Power Research Institute, Beijing, China. His main research area is power system planning.